Three-dimensional interface roughness in layered semiconductor structures and its effect on intersubband transitions

Alex Y. Song, Rajaram Bhat, Pierre Bouzi, Chung-En Zah, and Claire F. Gmachl

Three-Dimensional Interface Roughness in Layered Semiconductor Structures and Its Effects on Intersubband Transitions

Alex Y. Song,[1, 2, *] Rajaram Bhat,[3] Pierre Bouzi,[1] Chung-En Zah,[3] and Claire F. Gmachl[1]

[1]*Department of Electrical Engineering, Princeton University, Princeton, NJ 08540*
[2]*Department of Electrical Engineering, Stanford University, Stanford, CA 94305*
[3]*Corning Incorporated, Corning, NY 14831*

A general model for treating the effects of three dimensional (3D) interface roughness (IFR) in layered semiconductor structures has been developed and experimentally verified. The configurational average of the IFR potential produces an effective grading potential in the out-of-plane direction, which significantly alters the energy spectrum of the structure. The scattering self-energy of the 3D IFR is also derived. Under strong IFR, this scattering effect is shown to be dominant over phonon interaction and impurity scattering. When applied to intersubband transitions, these theoretical predictions explain the experimentally observed anomalous energy shift and unusual broadening in the intersubband transitions in III-Nitride superlattices.

Heterointerfaces are commonly found in a wide range of research fields[1–5]. They are frequently associated with significant interface roughness (IFR), for instance in III-nitride heterostructures, II-VI thin films including ZnSe or HgTe, perovskite quantum wells (QWs), and magnetic multilayers[6–10]. IFR plays an crucial role in the transport and optical characteristics of such structures. Traditional approaches to the effects of IFR are based on the premise of near-perfect interfaces. As such, a two-dimensional (2D) IFR random potential is assumed, which only appears on the ideal interface plane. Such a 2D approximation has been universally applied in studies ranging from condensed matter heterointerfaces to the Casimir effect[11–18]. In semiconductor samples with very high growth quality, a QW layer can even be regarded as adjoining regions of zero IFR.[19,20]. While these treatments are valid when IFR is sufficiently small, their general validity remains unverified. In the mean while, various interesting phenomena have been observed in the study of subband structures in QWs. Examples include anomalous intersubband (ISB) transition energy shift between experimental observations and theoretical predictions, unusual broadening in the ISB transition spectra, and topological phase transitions[1,8,21–29]. Understanding the subband structure and especially the role of 3D IFR is essential for further scientific study and device implementations[30]. Thus it is of interest to revisit the underlying theoretical model of IFR.

Here, we develop a model to accommodate IFR in the general 3D scenario. The generic stochastic form of the IFR potential with explicit 3D dependence is retained, i.e. dropping the 2D approximation. The configurational average of the IFR potential produces effective interface grading (EIG) on the lowest order, which significantly alters the energy spectrum. We also derive the IFR scattering self-energy for the general case. The IFR scattering is shown to be dominant over longitudinal optical (LO) phonon and impurity scattering when strong IFR exists. Such IFR scattering leads to extra broadening in the optical spectra. These predictions are confirmed by the experimental examination of ISB transitions in III-

nitride superlattices. This model also allows quantitative extraction of the roughness parameters.

We take a full quantum approach to the effects of 3D IFR within the framework of non-equilibrium Green's functions[31–33]. The model is explained as follows. The general Hamiltonian can be written as $H = H^0 + H^i + H^{ifr}$. The non-interacting H^0 includes the effective mass Hamiltonian within k·p theory[34], i.e. the superlattice potential assuming ideally smooth interfaces. The nonlinear spontaneous and piezoelectric polarization potentials are also contained in H^0. H^0 is separable and can be diagonized straightforwardly, whose eigen-system is known as the Wannier-Stark (WS) basis. The wave functions of a WS state is expressed as $1/\sqrt{A}e^{i\boldsymbol{k}\boldsymbol{r}}\psi_\mu(z)$, where the index μ represent the confined states in the out-of-plane direction z, $\boldsymbol{r}$ stands for the in-plane coordinates, and $\boldsymbol{k}$ represents the in-plane momentum. An example of such a structure is shown in Fig. 1 (left part, blue curves). The interacting term H^i includes the electron-phonon interaction, the impurity scattering and the electron-electron interaction, respectively. H^{ifr} represents the IFR random potential. The matrix element of H^{ifr} in the WS basis is denoted as $V^{ifr}_{\mu\nu}(\boldsymbol{k}, \boldsymbol{k}')$.

The characteristics of the structure are obtained by firstly solving the Dyson equation

$$
\begin{aligned}
&(\epsilon - h^0_{\mu\nu,\boldsymbol{k}} - h^{MF}_{\mu\nu,\boldsymbol{k}}) G^R_{\nu\boldsymbol{k},\mu'\boldsymbol{k}'}(\epsilon) \\
&= \delta_{\mu,\mu'}\delta_{\boldsymbol{k},\boldsymbol{k}} + (\Sigma^{e\text{-}ph}_{\mu\boldsymbol{k},\nu\boldsymbol{k}''}(\epsilon) + \Sigma^{imp}_{\mu\boldsymbol{k},\nu\boldsymbol{k}''}(\epsilon)) G^R_{\nu\boldsymbol{k}'',\mu'\boldsymbol{k}'}(\epsilon) \quad (1) \\
&\quad + (\Sigma^g_{\mu\boldsymbol{k},\nu\boldsymbol{k}''} + \Sigma^s_{\mu\boldsymbol{k},\nu\boldsymbol{k}''}(\epsilon)) G^R_{\nu\boldsymbol{k}'',\mu'\boldsymbol{k}'}(\epsilon)
\end{aligned}
$$

where ϵ is energy, h^0 is the matrix element of H^0, δ is the Kronecker delta and G^R is the retard Green's function. Repeated indices are summed. The self-energies Σ's are explained as follows. $\Sigma^{e\text{-}ph}$ and Σ^{imp} are the self-energies of electron-phonon interaction and impurity scattering, respectively. They contribute to the broadening of subband states and ISB transitions. They are calculated with the Fock-type diagram in the self-consistent Born Approximation (SCBA)[33]. The electron-electron Coulomb interaction is treated in the mean-field approximation, and the mean-field potential h^{MF} is calculated by
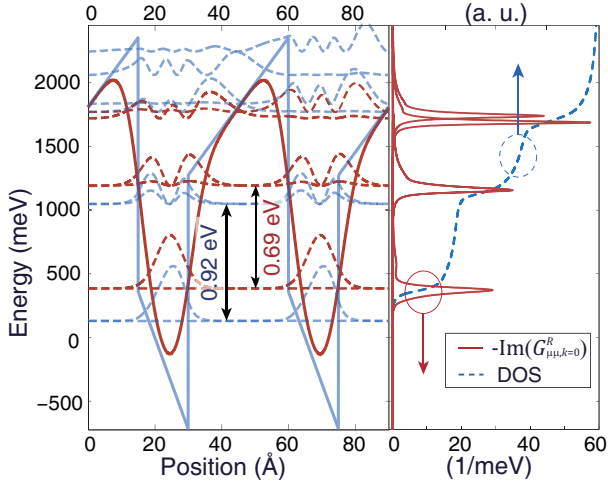
Figure 1. Subband structure of a 100-period GaN 1.5 nm / AlN 3 nm superlattice, with a Si doping of 1.6×10^{19} cm^{-3} in the wells. An Al$_{0.67}$Ga$_{0.33}$N template is employed. Left: the original superlattice potential (blue) and that containing Σ^g (red), assuming $\eta = 5.5$ Å and $\lambda = 7$ Å. The calculated wave functions of the WS and proper-WS states are also plotted (dashed). Right: $\Im(G^R_{\mu\mu,\boldsymbol{k}=0})$ and the total DOS obtained in the full calculation.

the Poisson equation

$$\partial_z^2 h^{MF}(z) = \frac{e}{\varepsilon} \left(2i \sum_{\mu,\boldsymbol{k}} \int \frac{d\epsilon}{2\pi} G^<_{\mu\mu\boldsymbol{k}}(\epsilon)\psi_\mu^2(z) - \rho_d(z) \right) \tag{2}$$

where ε is the permittivity, $G^<(\epsilon) = -2in(\epsilon)\Im G^R(\epsilon)$, $n(\epsilon)$ is the Fermi-Dirac distribution, and $\rho_d(z)$ is the density of the ionized impurities.

Σ^g and Σ^s in equation (1) are IFR originated self-energies:

$$\Sigma^g_{\mu\boldsymbol{k},\nu\boldsymbol{k''}} = \langle V^{ifr}_{\mu,\nu}(\boldsymbol{k}, \boldsymbol{k''}) \rangle \tag{3}$$

$$\Sigma^s_{\mu\boldsymbol{k},\nu\boldsymbol{k''}}(\epsilon) = \langle V^{ifr}_{\mu\alpha}(\boldsymbol{k}, \boldsymbol{k}_1) V^{ifr}_{\beta\nu}(\boldsymbol{k}_2, \boldsymbol{k''}) \rangle G^R_{\alpha\boldsymbol{k}_1,\beta\boldsymbol{k}_2}(\epsilon) \tag{4}$$

where the angle brackets $\langle \rangle$ are understood as the configurational average. Σ^g corresponds to the "single leg" diagram of random potential scattering. Σ^s is the scattering self-energy induced by IFR, which is handled within SCBA. The expressions of Σ^g and Σ^s depend on V^{ifr}.

Generically, the IFR stochastic potential V^{ifr} is a 3D function:

$$V^{ifr}(z, \boldsymbol{r}) = \sum_j \delta E_j (\theta(\tilde{z}_j - \xi_j(\boldsymbol{r})) - \theta(\tilde{z}_j)) \tag{5}$$

where δE_j is the band offset at the jth interface, z_j is the j's interface position, $\tilde{z}_j \doteq z - z_j$, θ is the Heaviside function, and $\xi_j(\boldsymbol{r})$ is the interface fluctuation at the in-plane location $\boldsymbol{r}$ of the jth interface. In (5) we retain the original form of the IFR stochastic potential with

explicit 3D dependence, and the approximation of a 2D IFR potential is dropped.

$\xi_j(\boldsymbol{r})$ is a Gaussian random process[35] with a probability distribution density $f_\xi(\zeta)$ and a correlation as

$$f_\xi(\zeta) = \frac{e^{-\zeta^2/2\eta^2}}{\sqrt{2\pi}\eta}, \quad \langle \xi_j(\boldsymbol{r}_1)\xi_j(\boldsymbol{r}_2) \rangle = \eta^2 e^{-r^2/\lambda^2} \tag{6}$$

where η is the roughness height, λ is the correlation length, and $r = |\boldsymbol{r}_1 - \boldsymbol{r}_2|$. Furthermore, the joint probability density at $\xi_j(\boldsymbol{r}_1) = \zeta$ and $\xi_j(\boldsymbol{r}_2) = \zeta'$ is

$$f^{(2)}_{\xi_j,r}(\zeta, \zeta') = \frac{1}{2\pi\sqrt{det(C)}} e^{-(\zeta,\zeta')C^{-1}(\zeta,\zeta')^T} \tag{7}$$

where $C = \eta^2(I + e^{-r^2/\lambda^2}\sigma_x)$ is the correlation matrix, I and σ_x are the identity matrix and the x-Pauli matrix, respectively.

With the original 3D form of IFR potential retained in (5), Σ^g can be expressed as[36]

$$\Sigma^g_{\mu\boldsymbol{k},\nu\boldsymbol{k''}} = V^g_{\mu\boldsymbol{k},\nu\boldsymbol{k''}} - V^0_{\mu\boldsymbol{k},\nu\boldsymbol{k''}} \tag{8}$$

where

$$\begin{aligned} V^g_{\mu\boldsymbol{k},\nu\boldsymbol{k''}} \\ V^0_{\mu\boldsymbol{k},\nu\boldsymbol{k''}} \end{aligned} = 4\pi^2 \delta_{\boldsymbol{k},\boldsymbol{k''}} \int dz \sum_j \delta E_j \frac{F_\xi(\tilde{z}_j)}{\theta(\tilde{z}_j)} \psi_\mu^*(z)\psi_\nu(z) \tag{9}$$

and $F_\xi(\tilde{z}_j) = (1 + erf(\tilde{z}_j/\sqrt{2}\eta))/2$ is the cumulative probability distribution. erf is the error function.

If a 2D IFR potential is assumed, the "single leg" diagram of Σ^g would produce a universal constant zero, thus has no physical effect. We recognize V^0 as precisely the unperturbed superlattice potential with ideally smooth interfaces. Σ^g can be merged into h^0, retaining the separability of the Hamiltonian. In the following, we call the basis formed by the eigenstates of $H^0 + \Sigma^g$ the "proper-WS" basis.

We have plotted an example of the superlattice potential added with Σ^g in Fig. 1 (left part, red curves). It is observed that the inclusion of Σ^g leads to an effective interface grading. As a result, the shape and the depth of the wells are reduced, causing a narrowing in the energy spacing between the proper-WS subbands.

Due to 3D IFR, the polarization charges at each interfaces are slightly distributed in z. This induces a small correction of ≤ 30 meV in the ISB transition energies in these samples[36]. For accuracy, we have included this effect in our calculation.

The IFR scattering self-energy Σ^s introduced in (4) plays a crucial role in the states broadening and the transport characteristics. It can also contribute to the energy renormalization of the subbands. Based on the 3D IFR stochastic potential, Σ^s can be expressed as[36]

$$\Sigma^s_{\mu\boldsymbol{k}\nu\boldsymbol{k''}}(\epsilon) = \int d^2\boldsymbol{p} \sum_j \frac{\delta E_j^2}{4\pi^2} \int d^2\boldsymbol{r} e^{-i\boldsymbol{p}\boldsymbol{r}} \iint dz dz'$$
$$\cdot sgn(zz') \iint_{(\zeta,\zeta')\in D} d\zeta d\zeta' f^{(2)}_{\xi,r}(\zeta,\zeta')$$
$$\cdot \mathcal{F}_{\mu\alpha\beta\nu}(z, z') \cdot G^R_{\alpha,\boldsymbol{k}-\boldsymbol{p},\beta,\boldsymbol{k''}+\boldsymbol{p}}(\epsilon) \tag{10}$$
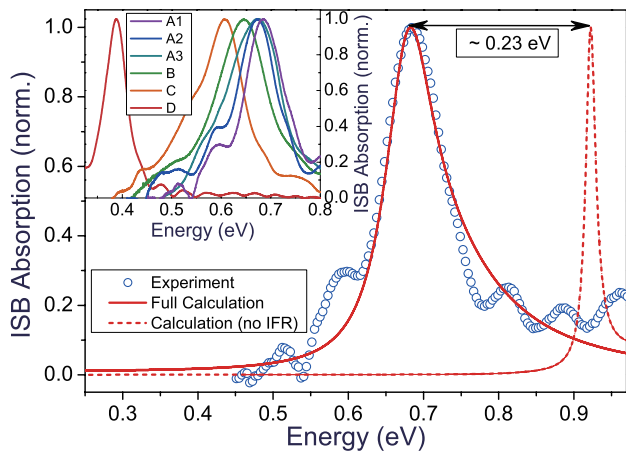
Figure 2. Blue circles: measured ISB absorption spectrum of design A1, obtained by dividing the transverse magnetic (TM) by the transverse electric (TE) absorption. Red solid and dashed curves: calculated ISB absorption spectrum of A1 with and without the effects of 3D IFR, respectively. Fitted roughness parameters of $\eta = 5.6\,\text{Å}$ and $\lambda = 4.3\,\text{Å}$ are used. Inset: normalized ISB absorption spectra of all designs at room temperature. Interference patterns are discernable in the spectra.

where $\mathcal{F}_{\mu\alpha\beta\nu}(z, z') = \psi_\mu^*(z)\psi_\alpha(z)\psi_\beta^*(z')\psi_\nu(z')$, $f_{\xi,r}^{(2)}(\zeta, \zeta')$ is the joint probability distribution found in (7), and the domain of integration is

$$D = \{ \begin{matrix} (-\infty, \tilde{z}_j), & \tilde{z}_j < 0 \\ (\tilde{z}_j, \infty), & \tilde{z}_j > 0 \end{matrix} \times \{ \begin{matrix} (-\infty, \tilde{z}_j'), & \tilde{z}_j' < 0 \\ (\tilde{z}_j', \infty), & \tilde{z}_j' > 0 \end{matrix} \quad (11)$$

To retrieve the energy structure of the superlattices, the Dyson equation (1) and the Poisson equation (2) are calculated iteratively. The calculated imaginary parts of the Green's functions $\Im(G_{\mu\mu, \mathbf{k}=0}^R)$ of the structure in Fig. 1 are also plotted in the right part of the figure. They represent the density of states (DOS) of the proper-WS subbands. The total DOS, $\sum_k 2\Im(G_{\mu\mu,\mathbf{k}}^R)$, is also plotted in Fig. 1. The staircase shape of the total DOS is a signature of a 2D system. The onset of each step corresponds to one proper-WS subband. Based on the full Green's functions, the ISB transition spectrum is generated by a conventional method, i.e. calculating the real part of conductivity using the Kubo formula[33,36,37]

For a systematic study of the effect of 3D IFR in the subband structure, we have designed, fabricated and characterized a series of GaN/Al(Ga)N superlattices with varying parameters listed in Table I. All samples are grown by metal organic chemical vapor deposition (MOCVD) on c-plane sapphire. Multi-layered templates are employed. The final template layer is strain relaxed $Al_xGa_{1-x}N$ with an Al composition matching the average value of the active layers, ensuring balanced strain in the superlattices. The average thickness of each layer is controlled within $\pm 3.5\%$ of the designed value. Multiple samples (≥ 3) are grown for one design to ensure repeatability. An experimental estimation of the rough-

ness height is obtained through characterization of the top surface morphology. To this end, atomic force microscope (AFM) measurements are performed at multiple locations on all wafers. An average roughness height of 6 Å is measured with a standard error of ± 2 Å.

Table I. III-nitride superlattice structures. The number of periods is 100. Si doping is introduced in the wells.

Sample	GaN (nm)	AlN (nm)	Doping ($\times 10^{19}$ cm^{-3})
A1	1.5	3.0	0.8
A2	1.5	3.0	1.6
A3	1.5	3.0	3.2
B	2.0	5.0	1.6
C	3.0	5.0	1.6
D	3.0	3.0 ($Al_{0.6}Ga_{0.4}N$)	0.8

In Fig. 2 we have plotted the calculated absorption spectrum of design A1 with (red solid curve) and without (red dashed curve) the IFR effects. The measured absorption spectrum is also shown (blue circles). The relevant material parameters used in the calculation can be found in Ref.[38]. The observed optical absorption only appears in the transverse magnetic polarization, which is a signature of ISB transition. The measured peak transition energy at 0.69 eV exhibits a redshift of 0.23 eV from the baseline calculation. In contrast, with the effects of 3D IFR included, the full calculation successfully reproduces both the peak transition energy and the broadening of the experimental result. In the inset of Fig. 2, we plot the measured ISB absorption spectra of all the designs in Table I. The peak transition energies span 0.39 eV - 0.69 eV. A summary of the measured peak energies (purple) and those calculated without considering the IFR effects (green) are shown in Fig. 3. As a demonstration of the effect of EIG, the ISB transition energies calculated with $H^0 + \Sigma^g + H^{MF}$ are also shown in Fig. 3 (red). A universally fitted roughness height of 5.5 Å is employed in the calculation. All measured ISB transitions exhibit clear redshifts of up to 25% compared to the results from the baseline calculation. The deviation in the average layer thickness of $\pm 3.5\%$ can only lead to an energy shift of less than ± 20 meV, which can not account for such a significant discrepancy. The electron-electron and electron-ionized impurity interactions in these structures merely contribute to ≤ 5 meV of energy shift in the subbands, thus is not the main reason for the observed discrepancy either. In the mean while, the calculation equipped with Σ^g immediately brings the predicted ISB transition energies close to the experimental results. This is a clear evidence of the effect of 3D IFR, since the conventional 2D approximation of IFR does not produce EIG at all.

The measured full widths at half maximum (FWHM) of the ISB transitions range from 50 meV to 150 meV (13% - 23% of the transition energy) in different designs. A summary is shown in the inset of Fig. 3. Such values are significantly larger than those found in the III-
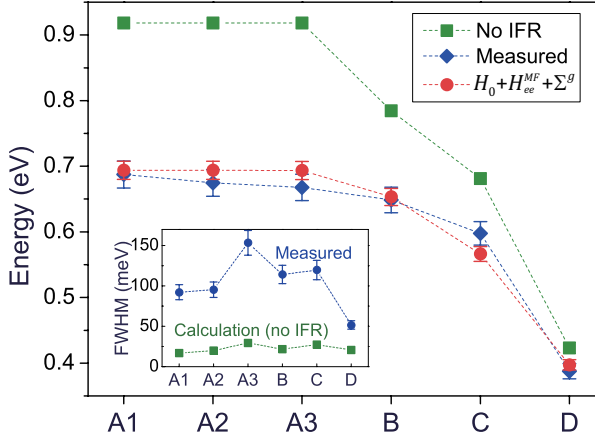
Figure 3. Green: calculated ISB transition energy without IFR effects for each design. Blue: Measured ISB peak transition energies. Red: calculation with $H^0 + \Sigma^g + H^{MF}$. Inset: Measured FWHM of the ISB transitions (purple) and that calculated without the effects of IFR (green).

Figure 4. Roughness heights η (red circles) and correlation lengths λ (blue triangles) obtained from fitting to the experimental absorption spectra. The shaded region represent the experimental estimation of the roughness height, 6 ± 2 Å.

Figure 5. Scattering lifetimes due to 3D IFR (red), LO phonons (green) and impurities (blue) for all designs. Units are given in both ps (right axis) and the corresponding energy in meV (left axis).

phosphide or -arsenide material system. As a comparison, the calculated FWHM's without the IFR effects are also plotted in the inset. The results are merely 20% - 40% of the measured values, clearly indicating the importance of the missing factor, the IFR scattering. With the full model developed above, one can extract the roughness height η and the correlation length λ in each sample by fitting the peak position and the FWHM of the ISB transition at the same time. A summary of the extracted η's and λ's are shown in Fig. 4. The experimental estimation of the roughness height η is also indicated in the shaded region. All fitted η's reside within the range of experimental result. For the correlation length λ, proper experimental measurement methods are still under discussion, with large uncertainty found in the reported values (14 Å $\sim$ 120 Å) in the more studied materials[35,39–41]. It is worthy to note that in our model the energy shift and the broadening provide two constraints, which enable simultaneous fitting of η and λ. The resulting λ's range from 4 Å to 10 Å. The variation among these samples is understandable since they have different structure designs and are grown on templates with different material compositions. The correlation lengths found here are generally smaller than those in III-phosphide or -arsenide materials. This is expected given that the interfaces in III-nitride materials are known to be considerably rougher.

In Fig. 5 we plot the semi-classical scattering lifetimes of IFR, LO phonon and impurities between the ground state and the first excited state at 300 K[32]. The plotted lifetimes take into account both the inter- and intrasubband scattering processes, which are responsible for the broadening of ISB transitions[37]. The LO phonon scattering lifetime includes contributions from both the phonon emission and absorption processes. As is shown, the LO phonon scattering lifetimes are typically $\sim$ 0.05 ps, while
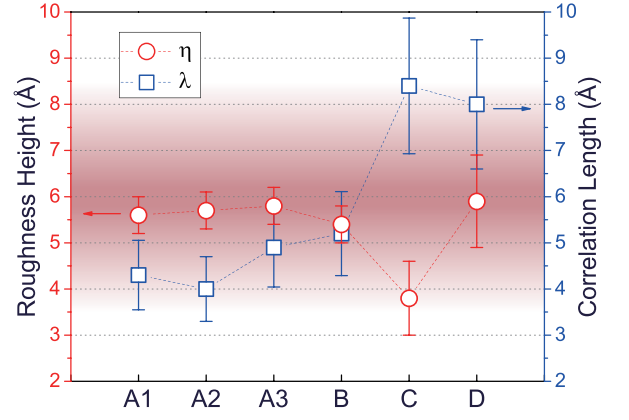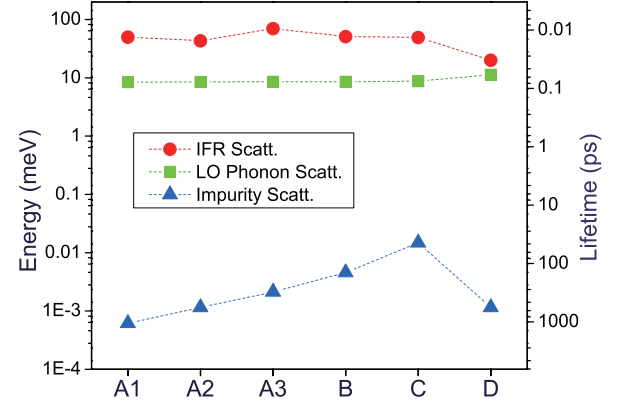
those of impurity scattering are $>$ 50 ps. Clear dominance of the IFR scattering of $\sim$ 0.01 ps is observed, which is a result of strong 3D IFR.

In summary, we have developed a general model for treating the effects of 3D IFR in layered semiconductor structures. Effective interface grading is predicted in the model, which significantly alters the energy spectrum. The IFR scattering self-energy is also derived for the general 3D case. It is shown to be dominant over phonon and impurity scattering. Through the full calculation, the anomalous energy shift and the unusual broadening in ISB transitions are explained. Beyond optical transitions, the results in this work are applicable to transport phenomena as well. This model is also extendable to other dimensional structures such as quantum wires and quantum dots. Equipped with the quantitative results of this work, mid-infrared ISB emission in III-nitride superlattices is realized[42].

ACKNOWLEDGMENTS

* alexys@stanford.edu

[1] M. S. Miao, Q. Yan, C. G. Van de Walle, W. K. Lou, L. L. Li, and K. Chang, Physical review letters **109**, 186803 (2012).

[2] H. Takagi, H. Kunugita, and K. Ema, Physical Review B **87**, 125421 (2013).

[3] M. König, S. Wiedmann, C. Brüne, A. Roth, H. Buhmann, L. W. Molenkamp, X.-L. Qi, and S.-C. Zhang, Science **318**, 766 (2007).

[4] P. King, R. He, T. Eknapakul, P. Buaphet, S.-K. Mo, Y. Kaneko, S. Harashima, Y. Hikita, M. Bahramy, C. Bell, et al., Physical review letters **108**, 117602 (2012).

[5] W. Kuch, L. Chelaru, F. Offi, J. Wang, M. Kotsugi, and J. Kirschner, Nature Materials **5**, 128 (2006).

[6] R. A. L. Almeida, S. O. Ferreira, T. J. Oliveira, and F. D. A. Aarão Reis, Physical Review B **89**, 045309 (2014).

[7] P. Boullay, A. David, W. Sheets, U. Lüders, W. Prellier, H. Tan, J. Verbeeck, G. Van Tendeloo, C. Gatel, G. Vincze, et al., Physical Review B **83**, 125403 (2011).

[8] C. Edmunds, L. Tang, M. Cervantes, M. Shirazi-HD, J. Shao, A. Grier, A. Valavanis, J. D. Cooper, D. Li, G. Gardner, D. N. Zakharov, Z. Ikonić, D. Indjin, P. Harrison, M. J. Manfra, and O. Malis, Phys. Rev. B **88**, 235306 (2013).

[9] N. Nakagawa, H. Y. Hwang, and D. A. Muller, Nature materials **5**, 204 (2006).

[10] J. Santamaria, M. E. Gómez, J. L. Vicent, K. M. Krishnan, and I. K. Schuller, Physical review letters **89**, 190601 (2002).

[11] F. Chevoir and B. Vinter, Physical Review B **47**, 7260 (1993).

[12] T. Ando, A. B. Fowler, and F. Stern, Rev. Mod. Phys. **54**, 437 (1982).

[13] T. Kotani, M. Arita, K. Hoshino, and Y. Arakawa, Applied Physics Letters **108**, 052102 (2016).

[14] R. Köhler, A. Tredicucci, F. Beltram, H. E. Beere, E. H. Linfield, A. G. Davies, D. A. Ritchie, R. C. Iotti, and F. Rossi, Nature **417**, 156 (2002).

[15] S. Tsujino, A. Borak, E. Muller, M. Scheinert, C. Falub, H. Sigg, D. Grutzmacher, M. Giovannini, and J. Faist, Applied Physics Letters **86**, 62113 (2005).

[16] A. Leuliet, A. Vasanelli, A. Wade, G. Fedorov, D. Smirnov, G. Bastard, and C. Sirtori, Physical Review B **73**, 085311 (2006).

[17] E. Lhuillier, I. Ribet-Mohamed, E. Rosencher, G. Patriarche, A. Buffaz, V. Berger, and M. Carras, Applied Physics Letters **96**, 061111 (2010).

[18] C. Deutsch, H. Detz, T. Zederbauer, A. M. Andrews, P. Klang, T. Kubis, G. Klimeck, M. E. Schuster, W. Schrenk, G. Strasser, et al., Optics express **21**, 7209 (2013).

[19] K. Brunner, G. Abstreiter, G. Böhm, G. Tränkle, and G. Weimann, Applied physics letters **64**, 3320 (1994).

[20] K. Leosson, J. R. Jensen, W. Langbein, and J. M. Hvam, Physical Review B **61**, 10322 (2000).

[21] L. Nevou, N. Kheirodin, M. Tchernycheva, L. Meignien, P. Crozat, A. Lupu, E. Warde, F. Julien, G. Pozzovivo, S. Golka, et al., Applied physics letters **90**, 223511 (2007).

[22] J. Heber, C. Gmachl, H. Ng, and A. Cho, Applied physics letters **81**, 1237 (2002).

[23] Y. Li, A. Bhattacharyya, C. Thomidis, T. D. Moustakas, and R. Paiella, Optics express **15**, 5860 (2007).

[24] D. Hofstetter, J. Di Francesco, D. Martin, N. Grandjean, Y. Kotsar, and E. Monroy, Applied Physics Letters **98**, 241101 (2011).

[25] C. Gmachl, H. M. Ng, and A. Y. Cho, Applied Physics Letters **77**, 334 (2000).

[26] H. Sodabanlu, J.-S. Yang, M. Sugiyama, Y. Shimogaki, and Y. Nakano, Applied Physics Letters **95**, 161908 (2009).

[27] N. Suzuki and N. Iizuka, Japanese journal of applied physics **38**, L363 (1999).

[28] N. Iizuka, K. Kaneko, and N. Suzuki, in *Lasers and Electro-Optics Society, 2004. LEOS 2004. The 17th Annual Meeting of the IEEE*, Vol. 2 (IEEE, 2004) pp. 665–666.

[29] E. Baumann, F. R. Giorgetta, D. Hofstetter, S. Golka, W. Schrenk, G. Strasser, L. Kirste, S. Nicolay, E. Feltin, J. Carlin, et al., Applied physics letters **89**, 041106 (2006).

[30] M. Lee, M. O. Hachiya, E. Bernardes, J. C. Egues, and D. Loss, Physical Review B **80**, 155314 (2009).

[31] A. Wacker and A.-P. Jauho, Phys. Rev. Lett. **80**, 369 (1998).

[32] S.-C. Lee and A. Wacker, Phys. Rev. B **66**, 245314 (2002).

[33] J. Rammer, Reviews of Modern Physics **63**, 781 (1991).

[34] M. Sugawara, N. Okazaki, T. Fujii, and S. Yamazaki, Phys. Rev. B **48**, 8102 (1993).

[35] J. B. Khurgin, Applied Physics Letters **93**, 091104 (2008).

[36] Please refer to the supplementary for details.

[37] T. Ando, Journal of the Physical Society of Japan **44**, 765 (1978).

[38] H. Morkoç, "Electronic band structure and polarization effects," (Wiley-VCH Verlag GmbH & Co. KGaA); J. Piprek, *Nitride semiconductor devices: principles and simulation* (John Wiley & Sons, 2007).

[39] A. Gold, Journal of Applied Physics **103**, 043718 (2008).

[40] D. Luhman, D. Tsui, L. Pfeiffer, and K. West, Applied Physics Letters **91**, 072104 (2007).

[41] D. N. Quang, N. H. Tung, L. Tuan, N. T. Hong, and T. T. Hai, Applied Physics Letters **94**, 072106 (2009).

[42] A. Y. Song, R. Bhat, A. A. Allerman, J. Wang, T.-Y. Huang, C.-E. Zah, and C. F. Gmachl, Applied Physics Letters **107**, 132104 (2015).